Applied Physics Letters

Experimental observations of topologically guided water waves within non-hexagonal structures

Cite as: Appl. Phys. Lett. **116**, 131603 (2020); https://doi.org/10.1063/1.5141850
Submitted: 08 December 2019 . Accepted: 06 March 2020 . Published Online: 01 April 2020

Mehul P. Makwana, Nicolas Laforge, Richard V. Craster, Guillaume Dupont, Sébastien Guenneau, Vincent Laude, and Muamer Kadic

Applied Physics Letters ARTICLE scitation.org/journal/apl

Experimental observations of topologically guided water waves within non-hexagonal structures

Cite as: Appl. Phys. Lett. **116**, 131603 (2020); doi: 10.1063/1.5141850
Submitted: 8 December 2019 · Accepted: 6 March 2020 ·
Published Online: 1 April 2020

View Online Export Citation CrossMark

Mehul P. Makwana,[1,2,a)] Nicolas Laforge,[3,b)] Richard V. Craster,[1,4,c)] Guillaume Dupont,[5] Sébastien Guenneau,[4] Vincent Laude,[3] and Muamer Kadic[3]

AFFILIATIONS

[1]Department of Mathematics, Imperial College London, London SW7 2AZ, United Kingdom
[2]Multiwave Technologies AG, 3 Chemin du Pre Fleuri, 1228 Geneva, Switzerland
[3]Institut FEMTO-ST, CNRS UMR 6174, Université de Bourgogne Franche-Comté, 25000 Besançon, France
[4]UMI 2004 Abraham de Moivre-CNRS, Imperial College, London SW7 2AZ, United Kingdom
[5]Aix Marseille Univ, CNRS, Centrale Marseille, IRPHE UMR 7342, 13013 Marseille, France

[a)]Electronic mail: mm107@ic.ac.uk
[b)]Electronic mail: nicolas.laforge@femto-st.fr
[c)]Author to whom correspondence should be addressed: r.craster@imperial.ac.uk

ABSTRACT

We investigate symmetry-protected topological water waves within a strategically engineered square lattice system. Thus far, symmetry-protected topological modes in hexagonal systems have primarily been studied in electromagnetism and acoustics, i.e., dispersionless media. Herein, we show experimentally how crucial geometrical properties of square structures allow for topological transport that is ordinarily forbidden within conventional hexagonal structures. We perform numerical simulations that take into account the inherent dispersion within water waves and devise a topological insulator that supports symmetry-protected transport along the domain walls. Our measurements, viewed using a high-speed camera under stroboscopic illumination, unambiguously demonstrate the valley-locked transport of water waves within a non-hexagonal structure. Due to the tunability of the energy's directionality by geometry, our results could be used for developing highly efficient energy harvesters, filters, and beam-splitters within dispersive media.

Considerable recent activity in wave phenomena is motivated through topological effects and focused on identifying situations where topological protection occurs that can enhance, or create, robust wave guidance along edges or interfaces. Remarkably, the core concepts that gave rise to topological insulators, originating within quantum mechanics,[2] are carried across, in part, to classical wave systems.[3,4] Topological insulators can be divided into two broad categories: those that preserve time-reversal symmetry (TRS) and those which break it. We concentrate upon the former due to the simplicity of their construction that solely requires passive elements. By leveraging the discrete valley degrees of freedom, arising from degenerate extrema in Fourier space, we are able to create robust symmetry-protected waveguides. These valley states are connected to the quantum valley-Hall effect, and hence, this research area has been named valleytronics.[5,6]

Hexagonal structures are the prime candidates for valleytronic devices as they exhibit symmetry induced Dirac cones at the high-symmetry points of the Brillouin zone (BZ); when perturbed, these Dirac points can be gapped, leading to well-defined KK' valleys distinguished, from each other, by their opposite chirality or pseudospin.

This pseudospin has been used in a wide variety of dispersionless wave settings to design valleytronic devices.[7,8] Here, we extend the earlier research by examining a highly dispersive physical system, i.e., water waves, and move away from hexagonal structures. The topological protection afforded by these valley states is attributed to, both, the orthogonality of the pseudospins and the Fourier separation between the two valleys.[9] The vast majority of valleytronics literature, inspired by graphene, opts to use hexagonal structures.[10–19] However, a negative that emerges with these, especially when dealing with complex topological domains,[9] is that certain propagation directions are restricted due to mismatches in chirality between incoming and outgoing modes. Notably, this has led to hexagonal structures being prohibited from partitioning energy in more than two directions.[13,14,16]

In this Letter, we demonstrate experimentally how a strategically designed square structure also allows for the emergence of valley-Hall edge states and for the excitation of modes that are not ordinarily ignited within hexagonal valley-Hall structures. Additionally, the system chosen differs from the vast majority of earlier literature[10–19] that has focused on an idealized situation in which the dispersion of the host medium has been avoided. This assumption restricts the applicability of the earlier studies to a small subset of, potentially useful, physical platforms that could host topological effects. Most notably, this assumption does not hold for water wave systems, which generally supports highly dispersive surface waves.[20] The combination of topological physics applied to water waves is a relatively unexplored area,[21,22] those who have conducted experiments have focused on either 1D systems[21] or the hexagonal valley-Hall structure.[22] Potential applications of this budding area include controlling ocean wave energy,[23] in a non-intrusive manner, for energy harvesting or erosion mitigation.[24]

The fluid within our domain has a constant depth of $h = 4\,\text{cm}$ and contains a periodic array of rigid, vertical, and bottom mounted, square objects (2 cm of side length in a 4 cm square array) that perforate the free surface of the liquid (see the experimental setup in Fig. 1). The planar coordinates are denoted by $\mathbf{x} = (x_1, x_2)$, while the vertical upward direction has the coordinate x_3; the origin is prescribed to be at the mean free surface. Under the usual assumptions of linear water wave theory,[20] where the fluid is assumed to be inviscid and incompressible with irrotational flow, there exists a velocity potential Φ[25] such that

$$\Phi(\mathbf{x}, t) = \Re e\left[\phi(\mathbf{x})\frac{\cosh(k(x_3+h))}{\cosh(kh)}\exp(-i\omega t)\right], \tag{1}$$

where ω denotes the angular frequency. The wavenumber, k, the real positive solution of the dispersion relation,

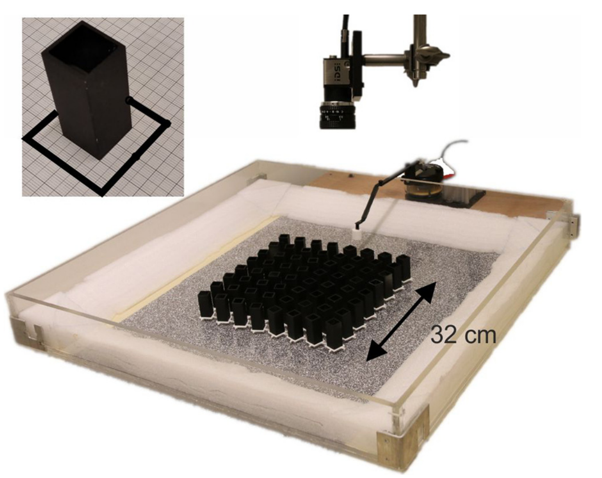

FIG. 1. Experimental setup: A crystal is assembled using square shaped aluminum tubes with a height of 7 cm arranged in a square array with different orientations using a plastic positioning frame at the bottom of the tank ($80 \times 80\,\text{cm}^2$ with 60° oblique edges made of soft polystyrene to mimic PMLs). A mechanical straight paddle holding a small plastic cylinder is used to generate water waves. The tank is continuously illuminated, and images of water waves are recorded using a high speed camera placed on the top. A black and white random pattern is placed under the tank to provide the water elevation measurement using an image cross correlation algorithm. The experimental setup was inspired by the work of Moisy *et al.*[1]

$$\left(gk + \frac{\sigma}{\rho}k^3\right)\tanh(kh) = \omega^2, \tag{2}$$

is used as a proxy for the frequency;[22] in Eq. (2), $g = 9.81\ \text{m s}^{-2}$ is the gravitational acceleration, $\sigma = 0.07\ \text{N m}^{-1}$ is the surface tension between air and water, and $\rho = 10^3\ \text{kg m}^3$ is the water density. Then ϕ, the reduced potential, satisfies the Helmholtz equation,

$$(\nabla_{\mathbf{x}}^2 + k^2)\phi(\mathbf{x}) = 0, \tag{3}$$

where this equation holds at the mean free surface and the subscript $\mathbf{x}$ indicates differentiation with respect to $\mathbf{x}$ and no-flow boundary conditions on the vertical rigid cylinders: taking $\mathbf{n} = (n_1, n_2)$ as the unit outward normal to the square tubes' surface, $\partial\phi/\partial\mathbf{n} = 0$ on each of them.

When the problem is posed in terms of the reduced potential, ϕ, as the Helmholtz equation, with periodically arranged inclusions (the tubes), this directly maps across to the phononic crystal literature. Recognizing the periodicity guides us to $\phi(x_1, x_2) = \phi_{\boldsymbol{\kappa}}(x_1, x_2)\exp(i\boldsymbol{\kappa}\cdot\mathbf{x})$, with $\boldsymbol{\kappa}$ being the Bloch wavenumber and $\phi_{\boldsymbol{\kappa}}$ being the periodic piece of the Bloch solution.[22] A key ingredient, which guides the experiments, is an understanding of the dispersion relation, relating k to the Bloch wavenumber, $\boldsymbol{\kappa}$ spanning the BZ $\boldsymbol{\kappa} \in [0;\pi/L]\times[0;\pi/L]$ [see Fig. 2(a)] for an infinite perfectly periodic square lattice system; we determine this relationship numerically. The geometry and band structures are shown in Fig. 2; for a square array, lattice constant L, the irreducible Brillouin zone (IBZ) is an eighth of the BZ. Despite this, we opt to plot around a quadrant of the BZ as this will incorporate the two distinct Dirac cones that are essential for our valley-Hall states. The desired quadrant has the following vertices: $X = (\pi/L, \pi/L)$, $N = (\pi/L, 0)$, $\Gamma = (0,0)$, $M = (0, \pi/L)$.

The chosen unrotated cellular structure, Fig. 2(a), contains, both, horizontal and vertical mirror symmetries along with fourfold rotational symmetry. Hence, in its entirety, the structure has C_{4v} point group symmetries. Notably, it is the presence of these mirror symmetries that yields Dirac cones along the outer edges of the BZ, Figs. 2(b) and 2(c).[26–30] Note that rectangular structures (wallpaper group $P2mm$) that possess these mirror symmetries will also yield these non-symmetry repelled Dirac cones.[27,28] In contrast to hexagonal structures, the position of these degeneracies can be tuned by varying the geometrical or material parameters of the system.[29] By rotating the internal square inclusion, both mirror symmetries are broken, thereby yielding the bandgap shown for the dispersion curves in Fig. 2(d). The residual valleys, which demarcate the bandgap, are locally imbued with a nonzero valley-Chern number,[31]

$$C_v = \frac{i}{2\pi}\int_S \nabla_{\boldsymbol{\kappa}} \times \phi_\kappa^*(\mathbf{x})\cdot\nabla_{\mathbf{x}}\phi_\kappa(\mathbf{x})d\boldsymbol{\kappa} = \frac{i}{2\pi}\oint_\gamma \phi_\kappa^*(\mathbf{x})\nabla_{\mathbf{x}}\phi_\kappa(\mathbf{x})\cdot d\mathbf{l}, \tag{4}$$

where the path integrated around (γ) encircles a particular valley and the superscript $*$ denotes the complex conjugate. Despite the calculation (and name) of C_v, resembling that of its TRS breaking counterpart, namely, the Chern number, there is an important difference: the former is not a quantized quantity, while the latter is. The surface associated with γ is not on a closed manifold, and hence, the Gauss–Bonnet theorem[32] does not hold. Despite this, the opposite pseudospin modes have a bijective relationship with $\text{sgn}(C_v) = \pm 1$,

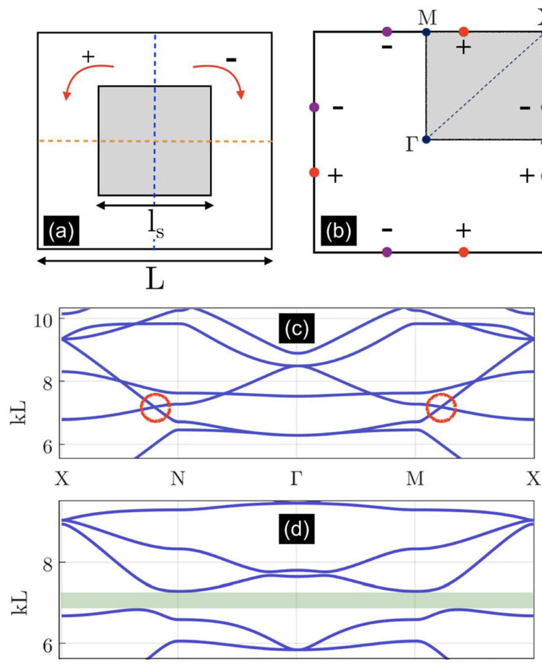

FIG. 2. Geometry, band structure, and topological features: (a) periodic cell (physical space) of the square lattice with sidelength L showing a square inclusion of sidelength l_s inside it. Mirror-symmetry breaking rotation (arrows) and lines (dashed) are also shown. (b) In reciprocal space, the points ΓNX denote the extrema of the IBZ that we extend to ΓNXM to show the two topologically inequivalent regions; the two distinct $\mathrm{sgn}(C_v)$ values are indicated by $\pm$ signs around the perimeter of the BZ, and these are associated with the $+$ perturbation in panel (a) (the—perturbation would result in opposite $\mathrm{sgn}(C_v)$'s, see Ref. 29) The $\mathrm{sgn}(C_v)$ positions resemble those in Refs. 27 and 28. (c) Band diagram for the configuration in (a), with two circles marking the position of the strategically engineered Dirac cones, (d) Band diagram when the inclusion is rotated through an angle of 20°. A bandgap highlighted in green emerges from the symmetry breaking perturbation at Dirac points.

which itself can be classed as a topological integer.[33] From this, we can apply the bulk-boundary correspondence for certain edge terminations, thereby guaranteeing the existence of valley-Hall edge states.

Motivated by this, we place a perturbed cellular structure, which contains a positively or negatively rotated inclusion, above its reflectional twin. This results in a pair of gapless edge modes that almost span the entirety of the bandgap, see Fig. 3. Here, we use "gapless" to refer to the crossing of the concave and convex (opposite parity) modes. This distinguishes valley-Hall systems, which are topological, from those that are not and have coupled edge states; for example, the armchair termination within hexagonal structures produces gapped edge states that are, in turn, less robust.[34]

The gapless nature of the states, and in turn the applicability of the Gauss–Bonnet theorem, is contingent upon the termination chosen that contains projections of valleys with identical $\mathrm{sgn}(C_v)$. Unique to this specific square structure, the different parity eigenmodes belong to the *same* interface (see Fig. 3), rather than different interfaces. Despite this, both, concave and convex states, have opposite parity and hence remain orthogonal. The relationship between the interfaces arises due to the mirror-symmetry relationship between the

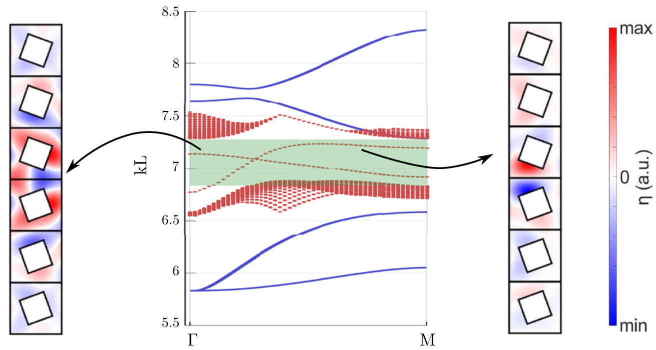

FIG. 3. Valley-Hall edge states: band diagram for a ribbon with the upper/lower inclusions rotated clockwise/anti-clockwise. The real parts of the even and odd eigenmodes within the bandgap are shown (in red) as are several close-by ribbon modes (also in red); the values of the latter range between their max and min, and a.u stands for arbitrary units (η is the vertical displacement of the surface). The blue curves are from Fig. 2(d), i.e., bulk modes along ΓM. Numerically, using finite elements, we take a long ribbon of N inclusions, apply Dirichlet boundary conditions to top and bottom, and extract the modes decaying away from the interface.

media on either side of the interface in Fig. 3. This also implies that a right-propagating mode along one of the interfaces is a left-propagating mode on the other. A numerical illustration of this phenomenon is found in Ref. 28, where decaying Hermite polynomials were used to oust a specific parity edge state, along both interfaces, non-simultaneously. This phenomenon does not occur for hexagonal structures where the different parity eigenmodes belong to different interfaces. This relationship between the two interfaces allows for propagation, within our square structure, which is ordinarily forbidden within graphene-like structures. Coupling between modes, which are hosted along different interfaces, is crucial for energy navigation around sharp corners[17] and within complex topological domains.[9,13,14,16] Further explanation for this phenomenon can be found in Refs. 27 and 28.

The propagation of water waves is imaged at the surface of the water tank shown in Fig. 1. A mechanical paddle holding a circular cylinder is shaken at a controllable frequency. Cylindrical waves originating from the monopolar source are observed numerically and experimentally in Figs. 4(a) and 4(e). The experimental setups for a topologically nontrivial interface, with two different lengths, are shown in Figs. 4(b) and 4(f); the upper/lower halves have square inclusions rotated clockwise/anti-clockwise in order to break the mirror symmetries and generate the valley-edge states required. Images were acquired using a high speed camera and post processed using a cross correlation algorithm[1] each image was discretized into 360 areas each composed of 16 pixels.

Full-wave numerical simulations, performed using COMSOL Multiphysics (a commercial finite element scheme), for tightly confined valley-Hall edge states, Figs. 4(c) and 4(d), show excellent agreement with the experiments, Figs. 4(g) and 4(h), despite our model not taking into account contact-line effects that occur between the water and the solid pillars, viscosity or nonlinearity. These square structure valley-Hall edge states have longer-wavelengths than their hexagonal counterparts, and hence, the distance between the pillars is subwavelength. A frequency modulated monopolar source is generated, which ignites the even-parity valley-Hall edge state. The observed patterns

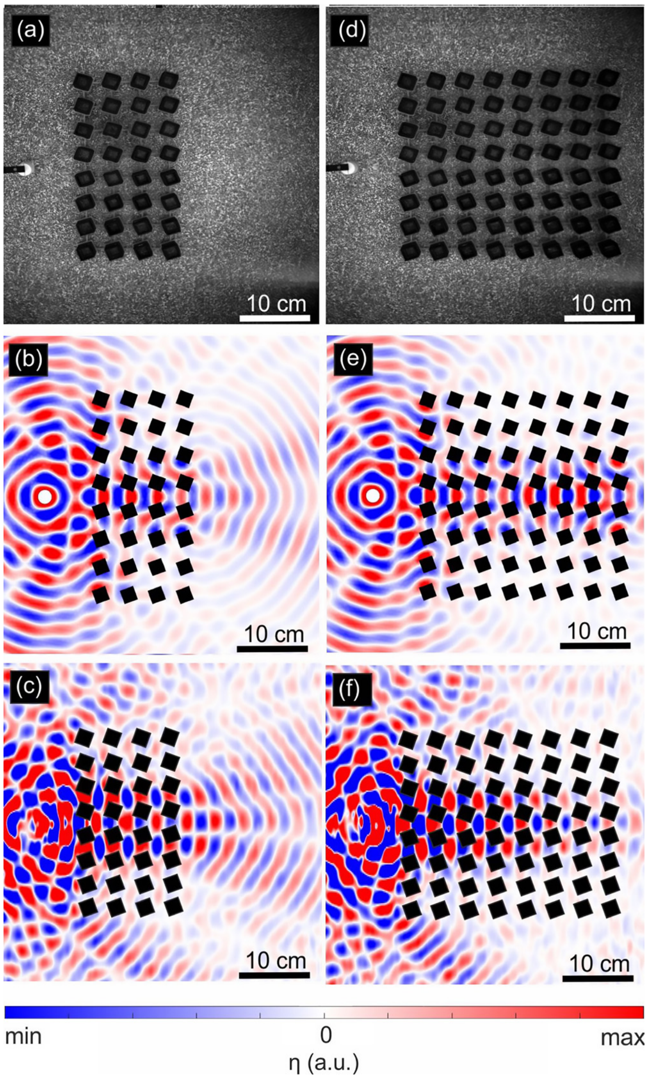

FIG. 4. Valley-Hall edge states: experiments and simulations. (a) and (d) Experimental setup showing the top view of the water surface perforated by 4×8 and 8×8 square rigid inclusions, respectively. (b) and (e) Corresponding numerical calculations; (c) and (f) experimentally observed wavepatterns. These valley-Hall states are generated by a monopolar source operating at a frequency of 7.3 Hz and placed 6 cm from the domain wall edge and propagate between inclusions rotated by $\pm 20°$.

are associated with the surface curvature where the colored regions are indicative of the vertical elevation of the water level. The localization of the topological edge state is clearly evident when comparing two interfaces of different lengths, i.e., four or eight squares in Figs. 4(c) and 4(f). Notably, the valley-Hall state that propagates across four columns, Fig. 4(c), radiates almost isotropically upon exit. In the absence of any rods, the energy would radiate isotropically away from the source. The broadbandedness of this effect is demonstrated via the experimental results shown in the supplementary material. The tight-confinement of these dispersive water waves, within a strategically designed square structure, is a highly nontrivial and unique observation.

We now strategically extend our earlier design, Figs. 4(b) and 4(f), to engineer four structured quadrants, which results in a three-way topological energy-splitter, Fig. 5. We rotate the bottom-right and top-right inclusion sets anti-clockwise and clockwise, respectively, thereby creating four distinct domain walls upon which the valley-Hall states reside. The monopolar source triggers a wave, from the leftmost interface, into upward and downward modes along with continuous rightward propagation. Incidentally, the most pronounced displacement pattern is along the two geometrically distinct horizontal interfaces. This continuous rightward propagation is *forbidden* for hexagonal systems.[9,13,14,16] For coupling between the incident mode and the right-sided mode, the chiralities must match and this does *not* happen for hexagonal structures. Contrastingly, this mismatch in chirality is overcome for the square structure as the right-sided interface is the reflectional partner of the left-sided interface. Hence, the incident mode needs only to couple to itself in order to continue its rightward propagation. This subtle relationship between the mirror-symmetry generated Dirac cones and the subsequent mirror-symmetry related interfaces allows for propagative behavior that is not readily found within the valleytronics literature, Fig. 5.

In the experiments, there are multiple loss mechanisms on the lengthscales that we are operating at, which are viscous attenuation,[36] contact line losses associated with the frictional drag of the meniscus moving up and down the rigid pillars, i.e., contact angle hysteresis,[35] Marangoni effects due to surface tension variations[37] and their effect on capillary-gravity waves, and then the nonlinear inertial effects that are ignored through linearization of the Navier–Stokes equations[20] Inspecting Fig. 5, which is a simulation, we note that the amplitude of the interface modes propagating up and down is about 1/10 of that propagating left to right. In Fig. 5(b), we insert losses, by lumping them into a complex wave velocity, of just 2% (we choose this to be simply illustrative and to demonstrate that losses can, in an experiment, obscure the subtle effects often sought in topological systems), and this reduces the signal quite dramatically in the up and down interfaces; in experiments, the amplitudes were too small to be accurately measured, and we attribute this to the loss mechanisms that we describe above.

We have experimentally shown the existence of topological valley-Hall transport for gravity-capillary water waves within a non-hexagonal structure. We have also simulated a three-way topological multiplexer for the same highly dispersive system and cautioned that

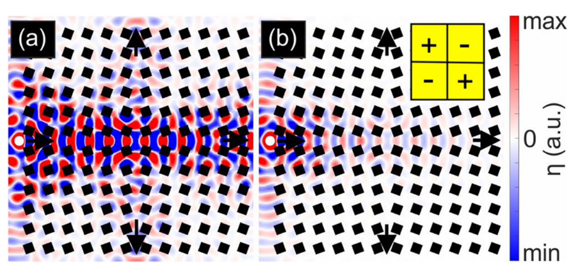

FIG. 5. Numerical illustration for a three-way splitter at 7.3 Hz: four quadrants of alternate squares rotated clockwise and counterclockwise. The valley-Hall phases, associated with the propagating modes, are shown within the yellow inset. (a) has no losses, while (b) incorporates attenuation introduced by considering a complex wave velocity with 2% imaginary part relative to the real part.

losses may lead to low amplitudes. These demonstrations open up a useful way for design in energy transport: the conventional symmetry constraints associated with hexagonal structures can be relaxed, leading to richer designs of waveguides and multiplexers within highly dispersive systems.

See the supplementary material for additional experimental images for valley-Hall edge states in crystals of different sizes. Also shown are images and simulations in the absence of the crystal. It also contains basic information about the finite element models used.

We acknowledge V. Pêcheur, E. Carry, T. Daugey, and F. Chollet for the experimental part. This work was supported by the EIPHI Graduate School (Contract No. ANR-17-EURE-0002) and by the French Investissements d'Avenir program, project ISITE-BFC (Contract No. ANR-15-IDEX-03). R.V.C. and M.P.M. thank the UK EPSRC for their support through Grant Nos. EP/L024926/1 and EP/T002654/1.

REFERENCES

[1]F. Moisy, M. Rabaud, and K. Salsac, "A synthetic Schlieren method for the measurement of the topography of a liquid interface," Exp. Fluids **46**, 1021 (2009).
[2]C. L. Kane and E. J. Mele, "Z2 Topological Order and the Quantum Spin Hall Effect," Phys. Rev. Lett. **95**, 146802 (2005).
[3]A. B. Khanikaev and G. Shvets, "Two-dimensional topological photonics," Nat. Photonics **11**, 763–773 (2017).
[4]T. Ozawa, H. M. Price, A. Amo, N. Goldman, M. Hafezi, L. Lu, M. Rechtsman, D. Schuster, J. Simon, O. Zilberberg, and I. Carusotto, "Topological photonics," Rev. Mod. Phys. **91**, 015006 (2019).
[5]K. Behnia, "Polarized light boosts valleytronics," Nat. Nanotechnol. **7**, 488–489 (2012).
[6]J. R. Schaibley, H. Yu, G. Clark, P. Rivera, J. S. Ross, K. L. Seyler, W. Yao, and X. Xu, "Valleytronics in 2D materials," Nat. Rev. Mater. **1**, 16055 (2016).
[7]J.-W. Dong, X.-D. Chen, H. Zhu, Y. Wang, and X. Zhang, "Valley photonic crystals for control of spin and topology," Nat. Mater. **16**, 298–302 (2017).
[8]D. Xiao, W. Yao, and Q. Niu, "Valley-contrating physics in graphene: Magnetic moment and topological transport," Phys. Rev. Lett. **99**, 236809 (2007).
[9]M. P. Makwana and R. V. Craster, "Designing multidirectional energy splitters and topological valley supernetworks," Phys. Rev. B **98**, 235125 (2018).
[10]C. He, X. Ni, H. Ge, X.-C. Sun, Y.-B. Chen, M.-H. Lu, X.-P. Liu, and Y.-F. Chen, "Acoustic topological insulator and robust one-way transport," Nat. Phys. **12**, 1124 (2016).
[11]H. Schomerus, "Helical scattering and valleytronics in bilayer graphene," Phys. Rev. B **82**, 165409 (2010).
[12]L. Ye, C. Qiu, J. Lu, X. Wen, Y. Shen, M. Ke, F. Zhang, and Z. Liu, "Observation of acoustic valley vortex states and valley-chirality locked beam splitting," Phys. Rev. B **95**, 174106 (2017).
[13]X. Cheng, C. Jouvaud, X. Ni, S. H. Mousavi, A. Z. Genack, and A. B. Khanikaev, "Robust reconfigurable electromagnetic pathways within a photonic topological insulator," Nat. Mater. **15**, 542 (2016).
[14]X. Wu, Y. Meng, J. Tian, Y. Huang, H. Xiang, D. Han, and W. Wen, "Direct observation of valley-polarized topological edge states in designer surface plasmon crystals," Nat. Commun. **8**, 1304 (2017).
[15]B.-Z. Xia, T.-T. Liu, G.-L. Huang, H.-Q. Dai, J.-R. Jiao, X.-G. Zang, D.-J. Yu, S.-J. Zheng, and J. Liu, "Topological phononic insulator with robust pseudospin-dependent transport," Phys. Rev. B **96**, 094106 (2017).
[16]Z. Qiao, J. Jung, Q. Niu, and A. H. MacDonald, "Electronic highways in bilayer graphene," Nano Lett. **11**, 3453–3459 (2011).
[17]M. P. Makwana and R. V. Craster, "Geometrically navigating topological plate modes around gentle and sharp bends," Phys. Rev. B **98**, 184105 (2018).
[18]K. Tang, M. P. Makwana, R. V. Craster, and P. Sebbah, "Observations of symmetry induced topological mode steering in a reconfigurable elastic plate," arXiv:1910.08172 (2019).
[19]M. Proctor, P. A. Huidobro, S. A. Maier, R. V. Craster, and M. P. Makwana, "Manipulating topological valley modes in plasmonic metasurfaces," arXiv:1909.12742 (2019).
[20]M. J. Lighthill, *Waves in Fluids* (Cambridge University Press, 1978).
[21]S. Wu, Y. Wu, and J. Mei, "Topological helical edge states in water waves over a topographical bottom," New J. Phys. **20**, 023051 (2018).
[22]N. Laforge, V. Laude, F. Chollet, A. Khelif, M. Kadic, Y. Guo, and R. Fleury, "Observation of topological gravity-capillary waves in a water wave crystal," New J. Phys. **21**, 083031 (2019).
[23]L. G. Bennetts, M. A. Peter, and R. V. Craster, "Graded resonator arrays for spatial frequency separation and amplification of water waves," J. Fluid Mech. **854**, R4 (2018).
[24]G. Dupont, F. Remy, O. Kimmoun, B. Molin, S. Guenneau, and S. Enoch, "Type of dike using C-shaped vertical cylinders," Phys. Rev. B **96**, 180302 (2017).
[25]C. M. Linton and D. V. Evans, "The interaction of waves with arrays of vertical circular cylinders," J. Fluid Mech. **215**, 549–569 (1990).
[26]W.-Y. He and C. T. Chan, "The emergence of Dirac points in photonic crystals with mirror symmetry," Sci. Rep. **5**, 8186 (2015).
[27]M. Makwana, R. Craster, and S. Guenneau, "Topological beam-splitting in photonic crystals," Opt. Express **27**, 16088 (2019).
[28]M. P. Makwana and G. Chaplain, "Tunable three-way topological energy-splitter," Sci. Rep. **9**, 18939 (2019).
[29]B.-Z. Xia, S.-J. Zheng, T.-T. Liu, J.-R. Jiao, N. Chen, H.-Q. Dai, D.-J. Yu, and J. Liu, "Observation of valleylike edge states of sound at a momentum away from the high-symmetry points," Phys. Rev. B **97**, 155124 (2018).
[30]J. Manzanares-Martinez, C. A. Romero-Ramos, and J. A. Gaspar-Armenta, "Dirac cone switching in two-dimensional photonic crystals by rotation of the crystal basis," Results Phys. **15**, 102748 (2019).
[31]T. Ochiai, "Photonic realization of the $(2+1)$-dimensional parity anomaly," Phys. Rev. B **86**, 075152 (2012).
[32]M. Berger and B. Gostiaux, *Differential Geometry: Manifolds, Curves, and Surfaces* (Springer-Verlag, 1988).
[33]K. Qian, D. J. Apigo, C. Prodan, Y. Barlas, and E. Prodan, "Theory and experimental investigation of the quantum valley Hall effect," arXiv:1803.08781 (2018).
[34]C. L. Fefferman, J. P. Lee-Thorp, and M. I. Weinstein, "Bifurcations of edge states—topologically protected and non-protected—in continuous 2D honeycomb structures," 2D Mater. **3**, 014008 (2016).
[35]J. F. Joanny and P. G. de Gennes, "A model for contact angle hysteresis," J. Chem. Phys. **81**, 552 (1984).
[36]J. C. Padrino and D. D. Joseph, "Correction of Lamb's dissipation calculation for the effects of viscosity on capillary-gravity waves," Phys. Fluids **19**, 082105 (2007).
[37]R. V. Craster and O. K. Matar, "Dynamics and stability of thin liquid films," Rev. Mod. Phys. **81**, 1131 (2009).